# Interface molecular engineering for laminated monolithic perovskite/silicon tandem solar cells with 80.4% fill factor.

*César Omar Ramírez Quiroz*[*‡1], George D. Spyropoulos[‡1], Loïc M. Roch[2], Michael Salvador[3], Marvin Berlinghof[4], José Darío Perea[1,2], Karen Forberich[1], Laura-Isabelle Dion-Bertrand[5], Nadine Schrenker[6], Andrej Classen[1], Nicola Gasparini[3], Ganna Chistiakova[7], Mathias Mews[7], Lars Korte[7], Bern Rech[7], Ning Li[1], Frank Hauke[8], Erdmann Spiecker[6], Tayebeh Ameri[1], Steve Albrecht[7], Gonzalo Abellán[8], Salvador León[2,9], Tobias Unruh[4], Andreas Hirsch[8], Alán Aspuru-Guzik[2,10], Christoph J. Brabec*[*1,11].

[1] Friedrich-Alexander University Erlangen-Nürnberg, Institute of Materials for Electronics and Energy Technology (I-MEET), Department of Materials Science and Engineering, Erlangen, Germany.

[2] Department of Chemistry and Chemical Biology, Harvard University, Cambridge, MA, USA.

[3] Kaust Solar Center, King Abdullah University of Science and Technology (KAUST).

[4] Institute for Crystallography and Structural Physics (ICSP), Department of Physics, Friedrich-Alexander-Universitty Erlangen-Nürnberg (FAU), Erlangen, Germany.

[5] Photon etc. Ltd, Montréal Québec, H2S 2X3, Canada.

[6] Friedrich-Alexander University Erlangen-Nürnberg, Center for Nanoanalysis and Electron Microscopy (CENEM), Department Werkstoffwissenschaften, Erlangen, Germany.

[7] Helmholtz-Center Berlin, Young Investigator Group for Perovskite Tandem Solar Cells, Berlin, Germany.

[8] Friedrich-Alexander University Erlangen-Nürnberg. Department of Chemistry and Pharmacy & Joint Institute of Advanced Materials and Processes (ZMP), Erlangen, German.

[9] Universidad Politécnica de Madrid, Departamento de Ingeniería Química, ETSIIM, Madrid. Spain.

[10] Canadian Institute for Advanced Research, Bioinspired Solar Energy Program, Toronto, ON M5G 1Z8, Canada.

[11] Friedrich-Alexander University Erlangen-Nuremberg, Bavarian Center for Applied Energy Research (ZAE Bayern), Erlangen, Germany.

* Correspondence should be addressed to:

*César Omar Ramírez Quiroz*
E-Mail: omar.quiroz@fau.de

## Abstract

We introduce a multipurpose interconnection layer based on Poly(3,4-ethylenedioxythiophene) doped with poly (styrene sulfonate), PEDOT:PSS, and D-sorbitol for the fabrication of monolithic perovskite/silicon tandem solar cells with high power conversion efficiency. The interconnection of independently processed silicon and perovskite sub-cells is a simple *add-on* lamination step, alleviating the common fabrication complexity of perovskite/silicon tandem devices. We demonstrate experimentally and theoretically that PEDOT:PSS is an ideal building block for manipulating the mechanical and electrical functionality of the charge recombination layer by controlling the microstructure on the nano- and meso-scale. We elucidate that the optimal functionality of the recombination layer relies on a gradient in the D-sorbitol dopant distribution that modulates the orientation of PEDOT across the PEDOT:PSS film. Using this modified PEDOT:PSS composite we show monolithic two-terminal perovskite/silicon tandem solar cell with a steady-state efficiency of 21.0%, a fill factor of 80.4% and negligible open circuit voltage losses. We envision that this lamination concept can be extrapolated for the pairing of multiple photovoltaic technologies, creating a universal platform that facilitates mass production of tandem devices with high power conversion efficiency.

**Keywords**

*Monolithic tandem, lamination, transparent-conductive-adhesive, perovskite/silicon, molecular dynamics, density functional theory.*

## Introduction

The stark research interest in perovskite photovoltaics has led to record lab scale power conversion efficiencies exceeding 22%[1]. It is the outstanding defect tolerance of perovskite semiconductors that allows to envision the design of technologies that uniquely combine solution-processing, reliability and cost effectiveness without compromising device efficiency, longevity and processability[2,3]. Nevertheless, the rapid growth of the global photovoltaic market, overwhelmingly owned by silicon-technologies, has imposed a significant economy-of-scale prize drop, making it difficult for new technologies to entering the market. On that account, recent studies estimate that reducing factory costs while further improving power conversion efficiencies will play a critical role for new technologies to achieve market readiness, enabling manufacturing to scale up more rapidly[4]. In this context, and as means to better match the solar spectrum and reduce thermalization losses, tandem solar cells represent an attractive technology (**Figure 1-a**). Recently, record efficiencies have been theoretically predicted and experimentally approached by merging silicon and perovskite technologies into a single monolithic tandem device[5,6]. However, the difficulty of the fabrication of this class of devices associated with the use of elaborate physical vapor deposition techniques such as atomic layer deposition and sputtering raises concerns about their potential for commercialization[5,6].

Given the complexity and number of functional layers, a major challenge in state-of-the-art two-terminal (monolithic) solar cell stacks is the electronic and processing compatibility of successive layers. It is therefore not surprising that the latest engineering advances revolve around layer-sequence tolerance and vertical process compatibility instead of high efficiency and economic feasibility[5,6].

Here, we report an innovative manufacturing process for perovskite/silicon two-terminal tandem solar cells, in which the two sub-cells can be developed and processed independently and afterwards electrically interconnected using a simple lamination process (**Figure 1b**). The key enabling technology is PEDOT:PSS(Poly(3,4-ethylenedioxythiophene):poly (styrene sulfonate)) doped with D-sorbitol, hereafter called D-PEDOT:PSS, functioning as both transparent conductive adhesive (TCA) and interconnection layer (ICL, **Figure 1-c,d**). This TCA provides mechanical adhesion as well as low resistivity and results in laminated perovskite/silicon tandem solar cells with high photovoltaic efficiency, on par with state-of-the-art devices. This result is particu-

larly exciting because the intermediate layer represents a sensitive link for achieving efficient optical and electrical coupling between the sub-cells being, generally, very challenging to combine optimal electrical conductivity, charge recombination behavior and layer compatibility in ICLs processed from solution.[7]

PEDOT based TCA's were first proposed as an alternative manufacturing method for light emitting diodes (LED's) and required a large concentration of organic compounds with multiple hydroxyl groups[8]. Substantial conductivity enhancements in combination with morphological rearrangements have been explored in PEDOT:PSS thin films featuring rather small amounts of co-solvents[9–13]. Of particular interest in bioelectronics applications are ionic and/or electronic transport properties and their connection to morphology upon addition of high-boiling point co-solvents[10–14 15]. Recently, several research groups followed up independently, where PEDOT:PSS-enabled TCAs are used exclusively for electrode lamination in single junction solar cells[16–19] and even modules[20]. However, the use of D-PEDOT:PSS as part of the interconnection layer of a monolithic tandem has not been explored before neither is the relation between morphology and electronic properties sufficiently understood. A fundamental understanding could introduce, as shown here, a simple yet effective solution for realizing hetero-tandem junction solar cells.

The application in a recombination layer imposes additional complexity and combining the two enabling functionalities of D-PEDOT:PSS into one layer may seem contradictory at first, as adhesion and conductivity are often conflicting properties. This is why the detailed function of the interconnection layer with more than 2 μm thickness, and specially the interplay between the conductive matrix (PEDOT:PSS) and the adhesive (sorbitol) has intrigued our attention. Through a combination of Raman and X-ray spectroscopy, we found evidence for a vertical gradient in the distribution of D-sorbitol that is directly linked to an increasing number of crystalline PEDOT aggregates at the critical interconnection interface and suggest that this finding is at the origin of the oxymoron between adhesion and conductivity that leads to high photovoltaic performance in laminated perovskite/silicon tandem cells.

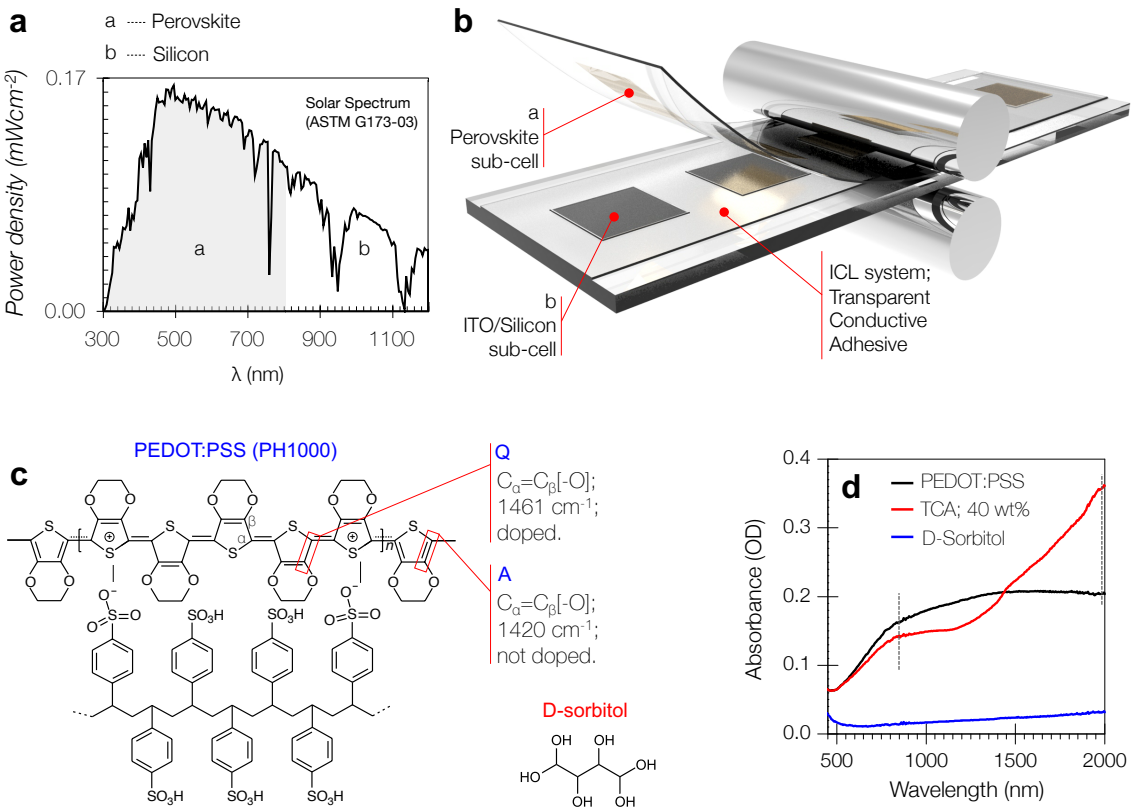


**Figure 1.** Solar spectral irradiance AM1.5G 1 (ASTM G173-03) showing complementary absorption between perovskite and silicon technologies, **a**. Schematic representation of the lamination process where the two sub-cells are pressed together to form a two-terminal perovskite/silicon tandem, **b**. Schematic representation of the aromatic and quinoid formation of the PEDOT structure upon doping, **c**. absorbance spectra of PEDOT:PSS and TCA showing difference in the polaronic (850 nm) and bipolaronic (2000 nm) bands upon addition of sorbitol, **d**.

### *Laminated two-terminal tandem solar cells*

The process for the fabrication of laminated two terminal perovskite/silicon tandem solar cells is illustrated in **Figure 1** and **Figure S1**, and can be summarized by the following steps.

Firstly, we utilized a silicon hetero-junction bottom cell with the following architecture: ITO / (p)a-Si:H / (i)a-Si:H / (n)c-Si wafer / (i)a-Si:H / (n)a-Si:H / ITO / Ti / Ag. We defined an active area of 15 $mm^2$ through an evaporation mask for the deposition of 40 nm indium thin oxide (ITO) as top contact layer. For the perovskite sub-cell, we utilized a p-i-n architecture with a re-

liably high fill factor, featuring a bilayer system for better extraction of holes from the perovskite absorber. A full discussion on the functionality of the hole transporting bilayer (HTL) is incorporated in the next section. The device area of the perovskite sub-cell was defined by means of laser patterning of ITO coated UV-fused silica substrates. We then developed *the interconnection layer (ICL) on top of the ITO of the silicon cell.* Our ICL consists of a thin mesh of nanostructured silver nanowires (AgNW; ~15 Ohm per square) followed by a blend of highly hole conductive (~1000 S $cm^{-1}$) PEDOT:PSS emulsion ink (Clevios PH1000; PEDOT to PSS ratio 1:2.5 w/w) with the addition of a significant amount of polyhydric alcohol (40wt% of D-sorbitol). 40wt% of D-sorbitol delicately balances the necessary mechanical and rheological properties for our deposition process. Notably, we did not observe a significant viscosity change of the PEDOT:PSS emulsion upon addition of D-sorbitol (from ~146 mPa $s^{-1}$ to ~150 mPa $s^{-1}$). Our ICL composite was deposited through doctor blading and the protocol was modified from previously reported work in our laboratories[20]. Next, *we laminated the two sub-cells to form a monolithic connection in series.* By simply pressing the perovskite sub-cell against the pre-annealed, ICL-coated silicon sub-cell, exerting a moderate pressure (~2 bars), we mechanically interconnected the PEI top layer of the perovskite sub-cell with the TCA layer on the silicon cell. The complete evolution of our ICL deposition method and lamination is discussed in the supportive information, and the full details of device fabrication are provided in the Methods Section.

The complete architecture of the laminated two terminal perovskite/silicon tandem device is depicted in **Fig. 2-a**. The steady-state *J-V* curve for the champion tandem device is shown in **Fig. 2-b** (solid black line, 4). The champion device yielded a power conversion efficiency of 21.0% under simulated solar illumination based on a $V_{oc}$ of 1.78 V, a FF of 80.4% and a $J_{sc}$ of 14.7 mA $cm^{-2}$. A complete collection of photovoltaic parameters along with the optimization process (**Figure 2-b, devices 1 – 3)** and the statistical metrics is presented in the supporting material (**Figure S2** and **Table S1**). The tandem device was held at maximum power point, under 1-sun simulated illumination, in air for up to 30 minutes without significant change in efficiency (**Fig. 2-b**, lower panel), i.e., the top and bottom substrates act as an inherent encapsulation barrier.

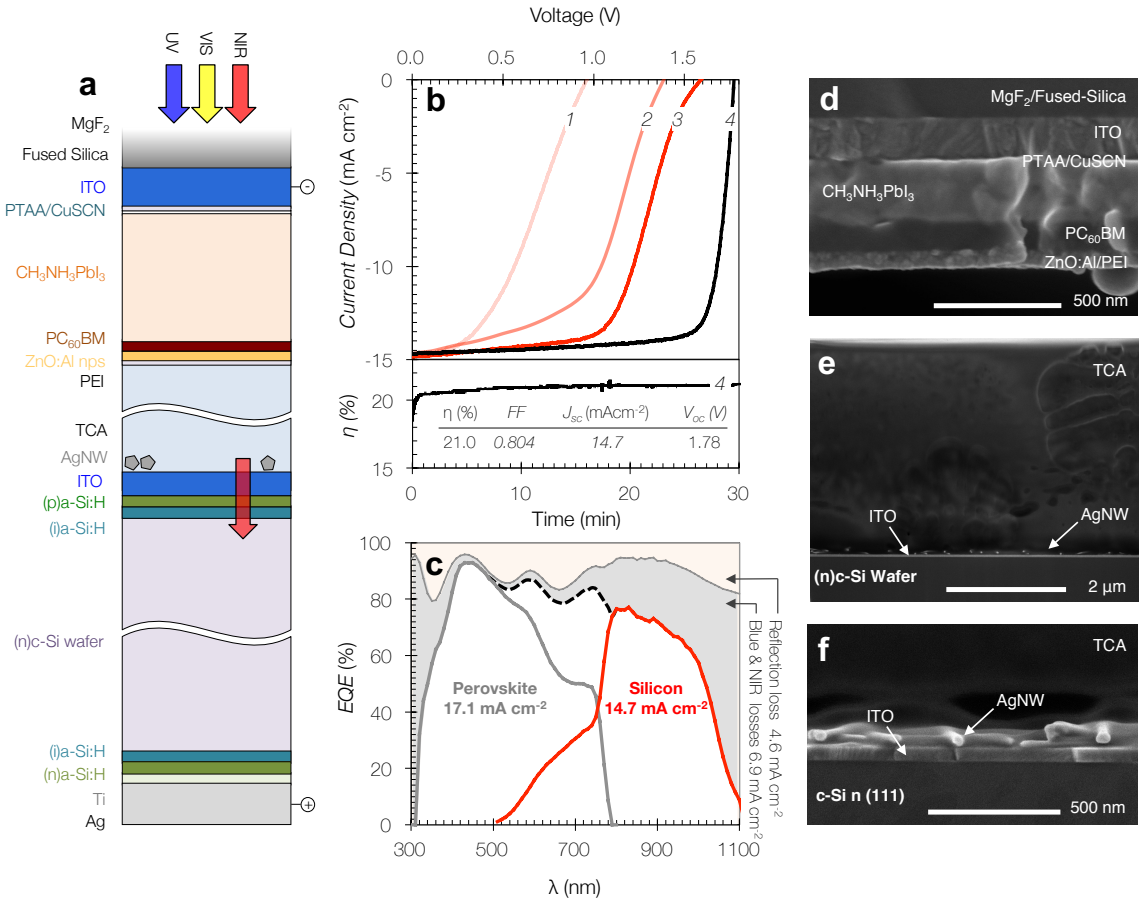


**Figure 2.** Two terminal perovskite/silicon tandem laminated through a transparent conductive adhesive (TCA) composite as interconnection layer, device architecture showing layer sequence, **a**. *J-V* curve and efficiency at maximum power point (lower panel) of the best performing device (black solid line labeled with the number 4). The *J-V* curves with labels 1 to 3 represent various stages the device optimization, **b**. Total device absorption (1-Reflection, thin-grey line), *EQE* from the silicon sub-cell is denoted by the red-solid line, the thick grey-solid is the *EQE* from the perovskite sub-cell. Grey and orange showed areas represent reflection and parasitic absorption losses, **c**. Cross-sectional SEM image of perovskite top sub-cell, **d**. Cross-sectional SEM of interconnection layer, the TCA composite is deposited on top of the silicon cell, **e**. Cross-sectional SEM of the ITO (from silicon sub-cell)/AgNW/TCA junction conforming the Silicon sub-cell side of the interconnection layer, **f**.

According to scanning electron microscopy (SEM) cross sectional micrographs, the thickness of the perovskite layer was ~240 nm (**Figure 2-d**). A close-up SEM micrograph shows the nanostructured AgNW mesh deposited atop the silicon sub-cell as a fundamental component of the ICL (**Fig 2-e, f)**. Furthermore, a SEM cross-section of the ICL as shown in **Fig. 2-e** demon-

strates that the TCA features an average thickness of ~2.8 μm. We have shown before that a D-PEDOT:PSS layer with such a thickness provides sufficient conductivity to efficiently extract charge carriers in a photovoltaic device[20].

In order to evaluate the spectrally resolved photocurrent generation under short circuit conditions, we measured the external quantum efficiency (EQE) of our perovskite/silicon tandem devices (**Fig 2-c**), following accepted standards[5]. We measured an integrated short-circuit current of 17.1 mA $cm^{-2}$ for the perovskite top-cell and 14.7 mA $cm^{-2}$ for the silicon bottom-cell. Furthermore, by recording the total reflectance of the device (thin grey line in **Fig 2-c**), we can quantify losses of short-circuit current, or prevention of those, associated with reflection and parasitic absorption. We found that, the utilization of $MgF_2$ as anti-reflection coating minimized the reflection losses to 4.6 mA $cm^{-2}$ (5.0 mA $cm^{-2}$ without the utilization of $MgF_2$). By inferring that the difference between the measured EQE and 1-Refleccion corresponds to the total parasitic losses of our device we can compute a total photocurrent loss of 0.9 mA $cm^{-2}$ for wavelengths below 700 nm, and 6.0 mA $cm^{-2}$ for wavelengths higher than 700 nm. Importantly, the parasitic loss associated with the ICL composite, including the TCA and the AgNW mesh, accounts for only ~10% of the total IR parasitic loss depicted in **Fig 2-c**.

We emphasize that one of the critical advantages of our process is that it allows for an independent development and optimization of the two photovoltaic sub-cells. This could in principle be explored for combining a variety of PV technologies and substrates, including flexible plastic substrates (**Fig. 1-b**). It is plausible that such an approach could improve the versatility of the fabrication process and reduce cost in the context of mass production.

***Single-junction perovskite solar cells with high Fill Factor***

It is important to briefly elucidate the design of the opaque single junction solar cell that lead to the aforementioned perovskite top-cell. The single junction perovskite solar cell with opaque back contact featured the following p-i-n architecture: $MgF_2$ (165 nm) / Fused silica / ITO (150 nm) / PTAA (~10 nm) / CuSCN (~5nm) / $CH_3NH_3PbI_3$ (~400 nm) / PCBM (~40 nm) / ZnO:Al nanoparticles (~40 nm) / PEI (~5 nm) Ag (~100 nm) (**Fig. 3-a**), where PTAA stands for poly[bis(4-phenyl)(2,5,6-trimethylphenyl)amine]. The rationale behind this device geometry was

to eliminate the performance loss that is commonly observed in connection with micrometer thick TCA composites – usually dominated by a reduced fill factor associated with an increase of the series resistance[17,20 18,19] – and thus to engineer perovskite sub-cell architectures with reduced transport related loss channels. As such, we selected PTAA as a hole transporting layer (HTL) as it allows the highest reported fill factors for perovskite architectures of up to ~84% [21–25]. Nevertheless, we observed a drop in open circuit voltage, raising concerns about the homogeneity of the PTAA layer[21]. Additionally, it was revealed that PTAA affords a rather slow extraction of holes, leading to recombination losses of first and higher order and limited charge collection[21]. To alleviate limited extraction of charge carriers through PTAA only, we further incorporated an ultrathin layer of CuSCN. CuSCN is an intrinsically p-doped high-bandgap semiconductor, with high hole mobility ($1.2x10^{-3}$ $cm^2V^{-1}s^{-1}$ *vs.* $1.2x10^{-5}$ $cm^2V^{-1}s^{-1}$ for PTAA[26,3]), good thermal stability and high transmittance[27]. The latter, along with its ideal refractive index (see **Fig. 3-a**), are desirable attributes for perovskite-preceding layers on tandem applications, as they will allow the transmission of infrared light across the device stack[3,28–30]. The combination of PTAA/CuSCN increased the fill factor considerably, from ~77% for PTAA alone to >82% on a 10.4 $mm^2$ active area configuration. Current-voltage characterization for both device architectures using PTAA and PTAA/CuSCN are displayed in **Fig. 3-b**, and extracted photovoltaic parameters can be found in the supplementary material (**Table. S2**).

We investigated in detail the optoelectronic properties of perovskite thin films in the presence of these different interfacial layers using steady-state and transient photoluminescence (PL) measurements as well as Fourier-transform photocurrent spectroscopy (FTPS). Clearly, the PL quenching efficiency and dynamics increase (**Fig. 3-d, e**) as does the spatial homogeneity of PL quenching across the perovskite film (**Fig. S3**). These measurements suggest that the presence of CuSCN on top of PTAA benefits the charge carrier extraction dynamics in a full device, most likely due to an efficient charge carrier transfer between the absorber and the selective contact[31,32]. Conversely, measurements of the Urbach energy – a measure for the degree of structural disorder of the perovskite material[33–36] – with (10.3 meV with $R^2$=0.999) and without CuSCN (10.4 meV with $R^2$=0.999) using FTPS reveal very low Urbach energies and no change in the crystallinity of near to ideally grown perovskite layers regardless of the underlying tem-

plate material. Overall, the hole transporting bi-layer PTAA/CuSCN provides improved optoelectronic attributes for single and tandem perovskite solar cell devices.

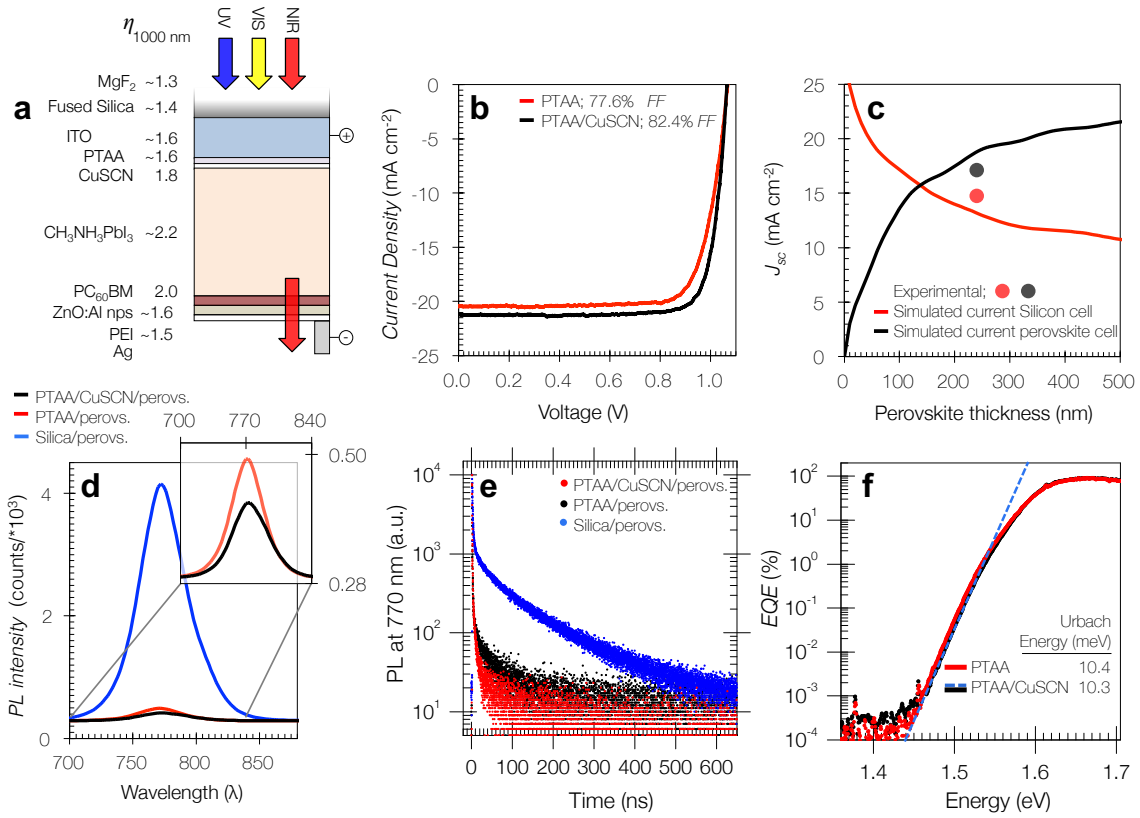


**Figure 3.** Perovskite sub-cell architecture showing the refractive index of each layer at 1000 nm, **a**. Representative photocurrent density-voltage curves under AM 1.5 irradiation at 0.1 Wcm$^{-2}$ illumination, **b**. Simulated and experimentally obtained photocurrent density of laminated perovskite/silicon monolithic tandem, **c**. Steady state photoluminescence of the perovskite semiconductor along with various extraction layers, **d**. Time-resolved photoluminescence decay measurements on perovskite films with and without intermediate CuSCN layer. The layers were excited by incident light from the glass side, **e**. The ratio of the area under the curve PTAA/PTAA-CuSCN was 1.47 for steady state PL (**d**) and 1.46 for transient PL (**e**). Comparison of the FTPS spectra of solar cells with PTAA only as well as with the implementation of the PTAA/CuSCN bilayer as hole extraction interface, **f**.

Returning to the device layout used for the opaque perovskite device (and top sub-cell), it is worth noticing that the device was finalized with a thin layer of PEI. This layer turns out to be crucial as it acts as a permeation barrier between the PEDOT:PSS containing TCA (silicon sub-cell) and zinc oxide nanoparticles (perovskite sub-cell, **Fig. 2a**) upon the lamination process, typically leading to reduced series resistance, in agreement with earlier reports[20]. Additionally, transfer matrix calculations of the current generation of bottom and top sub-cell as a function of the perovskite thickness and accounting for our ICL system show good agreement with our experimental results (**Fig 3-c**).

***Functionality, morphology and doping of interconnection layer***

The high FF of the laminated tandem raises the question of why such a thick, simultaneously adhesive and conductive PEDOT:PSS-D-sorbitol blend works so well as the interconnection layer of a monolithic tandem. We recall that PEDOT:PSS is a micro-dispersion of stable gel particles comprised by up to 95% water. The dispersed molecules are an ionically bonded, interlinked mixture of positively charged PEDOT oligomers and $PSS^-$ poly(anions) (**Fig. 1-c**). PEDOT itself is a hydrophobic oligomer with a typical number molecular weight distribution (Mn) in PEDOT:PSS dispersions ranging from 1,000 to 2,900 $gmol^{-1}$ (6 to 20 monomeric units per oligomer).[37] PSS, on the other hand, is a thermoplastic polymer with a typical Mn of about 400,000 $gmol^{-1}$ (**Fig. S4**).

The large hole conductivity of PEDOT:PSS is primarily a result of the $PSS^-$ poly(anion) doping of the π-conjugated electron system of PEDOT. Given that PEDOT is aromatic in the ground state and quinoid in the doped state, it is possible to characterize electronic transitions (polaronic or bipolaronic) in the PEDOT oligomers through optical absorption measurements[38–42]. **Figure 1-d** shows typical absorbance spectra for films fabricated using our PEDOT:PSS-sorbitol blend recipe (red), a pristine PEDOT:PSS emulsion (black) and a 40wt% sorbitol solution in deionized water (blue). All layers were fabricated as to afford similar thickness (~10 μm). The decrease of the polaronic band (850 nm) along with an increase of the bipolaronic band (2,000 nm) suggests that the addition of sorbitol enhances the doping efficiency of PSS, generating more highly doped PEDOT oligomers (**Fig. 1-d**)[9–11,42,43].

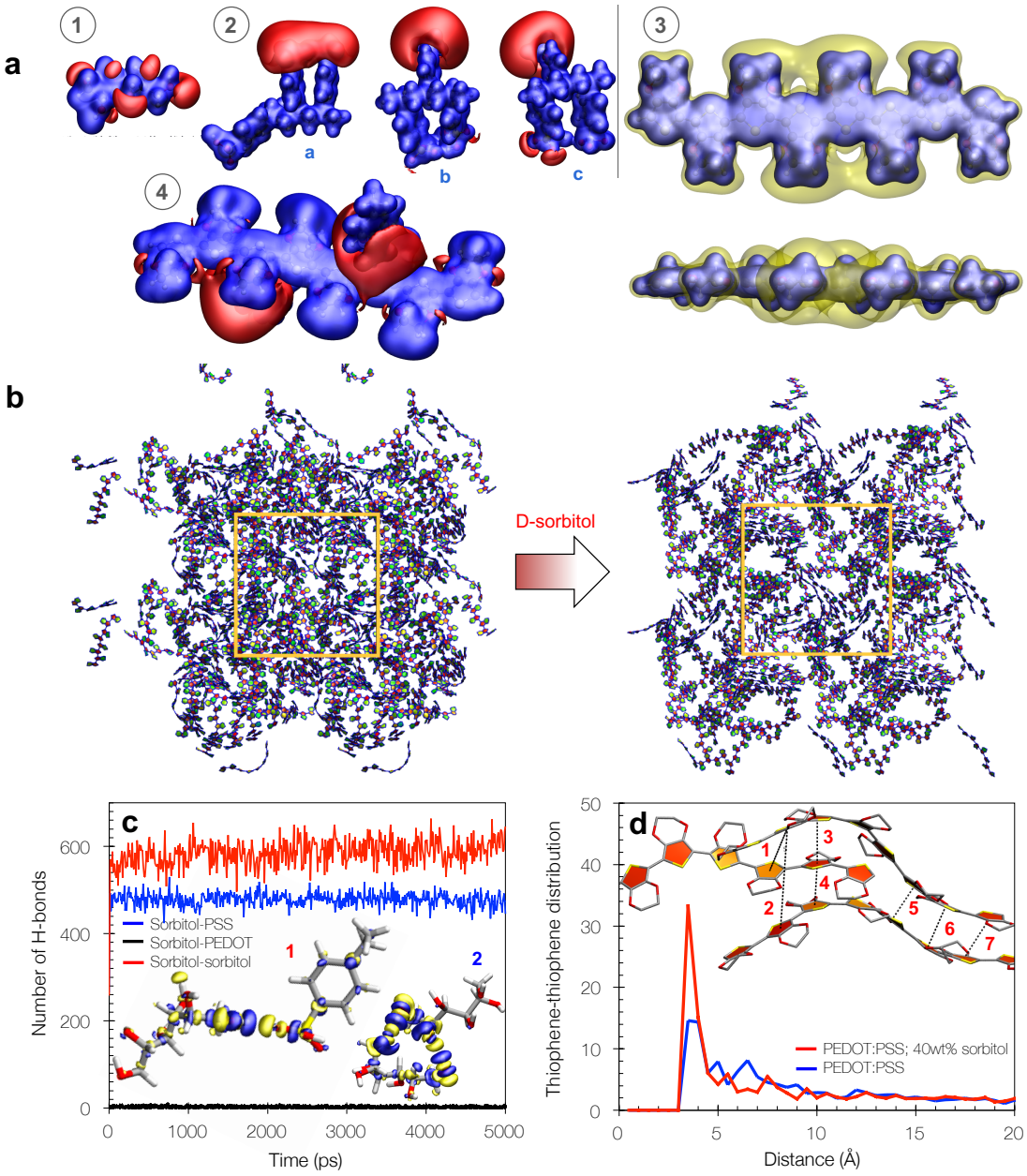


**Figure 4.** Molecular electrostatic potential counterplots of elements utilized on the molecular dynamics simulations. The threshold potentials in atomic units (a.u.) utilized are as follows: (1) D-sorbitol +0.05 & -0.03, (2) PSS trimer with different sequences +0.025 & -0.125, (4) most stable PEDOT:PSS structure +0.05 & -0.045, negative and positive potential are red and blue, respectively. (3) Corresponds to top and side view of $PEDOT^{2+}$ oligomers (8 units) +0.18 & +0.132 for the blue and yellow regimes, **a**. Four consecutive simulation boxes snapshot of the molecular dynamics for the systems PEDOT:PSS (left) and PEDOT:PSS 40wt% D-sorbitol (right). In order to effectively render the aggregation PEDOT upon addition of D-sorbitol, only the PEDOT oligomers are displayed, **b**. Number of hydrogen bonds during the molecular dynamics trajectory, inset shoes the total electronic density change upon the hydrogen formation, 1 sorbitol-sorbitol and 2 sorbitol-PSS, **c**. Radial distribution function between PEDOT thiophene rings upon addition of d-sorbitol, the inset shows a representation of three stacked PEDOT oligomers to illustrate the determination of the radial distribution function, **d**.

Noteworthy, the observed chromaticity of the PEDOT:PSS when reducing the absorption of the polaronic band will ultimately benefit the transit of light throughout the same wavelength regime of the Silicon sub-cell.

To gain a molecular understanding of the role of D-sorbitol in the doping mechanism of PEDOT:PSS, as evidenced by optical absorption measurements in the visible and near-infrared, we performed classical molecular dynamic (MD) simulations of the PEDOT:PSS system in the presence of D-sorbitol. The atomic charges used for the parametrization of the classical MD simulations were obtained from the molecular electrostatic potential (MEP; for detailed information, we refer the reader to the supplemental material). This is shown in **Figure 4-a,** (from 1 to 4) for the individual components sorbitol (1), PSS (2), PEDOT (3) and for PEDOT:PSS (4). For PEDOT:PSS (4), we defined a chain comprised of 8 monomeric units and 2 positive charges (bipolaron). As model compound for PSS, we considered a trimer with a negatively charged central unit, i.e., SSH–$SS^{-}$–SSH. Furthermore, a total of 100 starting structures, consisting of two $PSS^{-}$ pentamers and a single 8-unit $PEDOT^{2+}$ chain, were generated in the case of PEDOT:PSS. Structure (4) **Figure 4-a** depicts the most stable complex along with its charge distribution.

The calculation of the MEP revealed several important aspects. For instance, in the case of PEDOT the charge density close to the nuclei is uniformly spread along the PEDOT chain (core MEP in blue) and is, therefore, not impacted by the missing electrons, though some charge is concentrated around the 4 central units of PEDOT (yellow counterplot). The scenario in the case of PSS is particularly relevant. Considering the three most probable structures (**Figure 4-a,** (3; a to c)), the calculations show that the negative charge is primarily located on the central SS-unit. In one case (3a), the negative charge is, however, delocalized over two SS subunits, although the central unit is more negative. We rationalize this observation by concluding that the proton of the neutral subunit is weakly bound to both of the SS subunits. More specifically, the hydrogen atom forms a weak covalent bond with the neutral PSS subunit (bond length of 1.12 Å) and a strong H-bond with the negative PSS subunit (H-bond length of 1.33 Å). As a reference, the typical O-H bond length in a $SO_3H$ group is computed to be 0.98 Å at the same level of theory.

Upon the conclusion of the parametrization, we proceeded with the MD simulations. **Figure 4-b** shows MD renderings of the PEDOT-PSS system, visualizing the spatial distribution of the PEDOT oligomers in the pristine system (left), and with a 40% content of D-sorbitol (right) (MD snapshots for all other components can be seen in **Figure S5**). The analysis of the hydrogen bond interactions in this rendering provides insight into the role of D-sorbitol on the morphology of D-PEDOT:PSS. **Figure 4-c** shows the number of hydrogen bonds formed by sorbitol over time during the MD simulation. As expected, there are almost no hydrogen bonds formed between sorbitol and PEDOT. This is explained by the repulsive potential of $PEDOT^{2+}$ (**Figure 4-a** (3)), precluding hydrogen atoms to approach. However, a large number of hydrogen bonds are formed between sorbitol and $PSS^-$ as well as among sorbitol molecules. As a matter of fact, with up to ca. 500 H-bonds for a total of 640 PSS repeat units present in the simulation box, the proportion of hydrogen bonds with sorbitol is about 0.8 per PSS unit. Representative H-bonds for sorbitol-sorbitol and for sorbitol-PSS, along with their respective total electronic density change are rendered in the inset of **Figure 4-c**. To investigate whether the formation of hydrogen bonds between PSS and sorbitol has an impact on the PEDOT-PSS interaction, and on the arrangement of the PEDOT units, it is of interest to analyze the radial distribution function between the PEDOT groups. To get a more lucid picture, the distribution function is computed between the closest centers of thiophene rings in different PEDOT chains (that is, only the shortest distance between two given chains is considered) with and without D-sorbitol, as depicted in the inset of **Figure 4-d**. Both profiles display a maximum at 3.65 Å, a distance close to the experimental π-π stacking distance, as discussed below. Interestingly, the intensity of that peak is more pronounced when 40% sorbitol is mixed with the PEDOT-PSS system, and, thus sorbitol appears to favor the stacking of PEDOT. The peak observed at 7.30 Å corresponds to the formation of the trimer. The intensity is much lower, implying that PEDOT aggregates consist of mostly two stacked chains; it is also broader, indicating a dispersion of the separation between pairs. This observation is also reflected at the quantum mechanical level and is explained by considering the electrostatic repulsion between the positively charged 8-unit PEDOT chains. We conclude this section by summarizing that the doping mechanism of D-sorbitol is of indirect nature. D-sorbitol does not directly dope PEDOT. Instead, D-sorbitol forms hydrogen bonds with the PSS units, while being repulsed by charged PEDOT units, overall enhancing dimer formation of charged PEDOT oligomers.

While the computation of molecular dynamics provides insight on a molecular level, for a global device understanding it is important to elucidate whether D-sorbitol acts uniformly across the thickness of the TCA layer (>2 μm). We thus performed resonance statistical Raman spectroscopy (SRS) to assess the electronic structure evolution of PEDOT upon doping[9,44,45]. This can be done by monitoring the symmetric stretching bond $C_{\alpha}=C_{\beta}$*[-O]* of the thiophene in PEDOT (**Fig. 1-c**). As a result of the disruption of the π-conjugated bond sequence upon doping (see **Fig. 1-c**), the main aromatic-symmetric $C_{\alpha}=C_{\beta}$*[-O]* stretching mode will undergo two main changes: a frequency shift towards higher wavenumbers, and a band splitting[46]. Hence, a ratio between the split quinoid-symmetric $C_{\alpha}=C_{\beta}$*[-O]* stretching band and the main aromatic-symmetric $C_{\alpha}=C_{\beta}$*[-O]* stretching band is inferred to as a figure-of-merit for the doping ratio of the PEDOT oligomer[44–48]. We utilized an excitation wavelength of 785 nm to maximize band intensity by directly exciting resonant to the polaron absorption. The resulting mean Raman spectra (average of at least 100 single point spectra measured along a surface area of 10 $\mu m^2$) presented in **Figure 5-a** show clear symmetry alterations in the electronic structure of PEDOT:PSS upon co-solvent induced doping[9,45,48]. An overview of the observed vibrational modes obtained by spectra deconvolution can be found in the supporting material (**Figure S6** and **Table S4**). Our results show a shift of the main aromatic-symmetric $C_{\alpha}=C_{\beta}$*[-O]* (A-Band) stretching mode from 1420 $cm^{-1}$ to 1429 $cm^{-1}$ upon the addition of sorbitol and a subsequent increase of the split quinoid-symmetric $C_{\alpha}=C_{\beta}$*[-O]* stretching band (Q-Band; shoulder in **Fig. 5-a**) by a factor of ~2.6 according to a curve fitting analysis and in agreement with the occurrence of doping. Given the considerations of the MD simulations, both Raman spectroscopy and MD simulations together suggest that addition of sorbitol stimulates segregation of PEDOT from PSS polymeric sections. Driven by a strong PSS-to-sorbitol H-bonding formation rate, this segregation will translate into PEDOT-rich and PSS-rich domains. While segregating, the overall enhanced molecular alignment will increase the proximity between un-doped PEDOT and PSS monomeric units. Hence, the ionic interactions between PEDOT and PSS will increase in frequency leading to the observed evolution of the quinoid-doped chemical structure of the PEDOT-monomer.

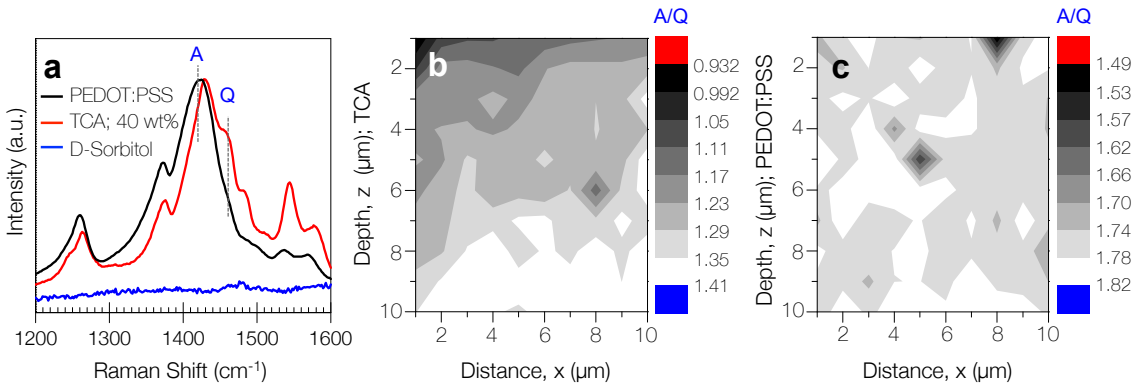


**Figure 5.** Statistical Raman spectrograms (785 nm excitation) of PEDOT:PSS and TCA highlighting the increase in PEDOT-quinoid species upon sorbitol addition. Label A indicates the aromatic-symmetric $C_\alpha$=$C_\beta$*[-O]* stretching band, while the label Q indicates the quinoid-symmetric $C_\alpha$=$C_\beta$*[-O]* stretching band. A minimum of 100 spectra along a surface area of 10 μm$^2$ (1 μm step size) where averaged for each plot, **a**. Depth-resolved scanning confocal Raman microscopy analysis highlighting the $C_\alpha$=$C_\beta$*[-O]*/$C_\alpha$=$C_\beta$*[-O]* (A/Q) ratio distribution in TCA and PEDOT:PSS, **b** and **c**, respectively.

Using confocal scanning Raman microscopy, it is possible to gain depth-resolved information on the ratio of the A- and Q- bands and thus draw a profile of the degree of doping across the PEDOT:PSS-sorbitol layer. By gradually moving the focus of the excitation laser throughout the sample we were able to resolve individual planes at a micrometer level resolution. **Figure 5-b** and **Figure 5-c** show depth-resolved mappings of the absolute Raman intensity ratio between the A-band and the Q-band for a TCA and a pristine PEDOT:PSS film, respectively. This representation clearly unveils a doping gradient towards the film surface in the case of the TCA. Such a gradient is not observed in the case of bare PEDOT:PSS. When implemented in the perovskite/silicon tandem, the top of the TCA (silicon side) will be in direct contact with PEI (perovskite side). We propose that the presence of D-sorbitol at the top promotes the necessary mechanical adhesion for achieving good electrical contact, a requirement towards an effective interconnection layer. We note that the evolution of the overall photovoltaic performance shown in **Fig. 2-b** is directly linked to the optimization of the processing of the TCA film, which is detailed in the supplementary information.

To confirm the conformational gradient observed with resonance Raman spectroscopy, we analyzed the top and bottom of thin film samples of TCA and PEDOT:PSS using grazing-incidence

wide angle X-ray scattering (GIWAXS)[49]. GIWAXS is particularly suitable because it provides information on the microstructure of thin films with limited scattering depth. The scattering depth at the highest measured outgoing angle was calculated to be ~2.4 µm and ~2.2 µm for PEDOT:PSS and TCA, respectively. In order to probe the bottom side, pre-thermally treated films of ~8 µm thickness were transferred upside down onto single crystalline silicon substrates. **Figure 6** shows the radial integrated scattered intensity signal extracted from GIWAXS scans (**Fig. S7**) of pristine PEDOT:PSS and D-PEDOT:PSS. As a reference, **Figure 6-a** depicts the characteristic π-π stacking peaks of PSS ($Q$ = 12.3 $nm^{-1}$) and PEDOT ($Q$ = 17.8 $nm^{-1}$)[13,14,41,50,51], while **Figure 6-d** compares those signals for D-PEDOT:PSS films probed from the top (**Fig. 6b**) and the bottom (**Fig. 6c**) after Gaussian deconvolution of the scattering signals (see SI for details). Importantly, the intensity of both π-π stacking peaks is higher when probed from the top (**Fig. 6d**). The PEDOT π-π stacking intensity is, however, significantly higher than the PSS π-π stacking intensity. From the MD simulations, we know that D-sorbitol favors the stacking of PEDOT (**Fig. 4c**). There is thus a direct link between the compositional gradient observed with scanning Raman microscopy and the conformational gradient probed with GIWAXS, with accumulated D-sorbitol inducing a higher degree of molecular orientation of PEDOT chains (or an increasing number of crystalline aggregates) when approaching the top of the TCA film. Conversely, when comparing the PEDOT scattering peak centers of TCA-top and TCA-bottom, we did not observe any significant change in terms of π-stacking distances or peak width: $Q$ (TCA-bottom) = ~1.79 $Å^{-1}$ (3.51 Å stacking distance) and $Q$ (TCA-top) = ~1.80 $Å^{-1}$ (3.49 Å stacking distance). The latter entails the existence of crystalline aggregates comparable in size and packing distance across the TCA. Additionally, both TCA-top and TCA-bottom showed an average ~30% narrower width, as compared with the pristine PEDOT:PSS, indicating on average a higher degree of PEDOT ordering upon addition of sorbitol.

Overall, the implication of a conformational gradient across the TCA film can be ascribed to a macroscopic diffusion of sorbitol towards the top interface. A more doped top–TCA interface is likely to improve mechanical adhesion followed by enhanced physical adsorption, thus, forming an electrical contact with low interconnection losses in laminated hybrid perovskite/silicon tandem solar cells, as demonstrated through a high fill factor and overall high photovoltaic performance.

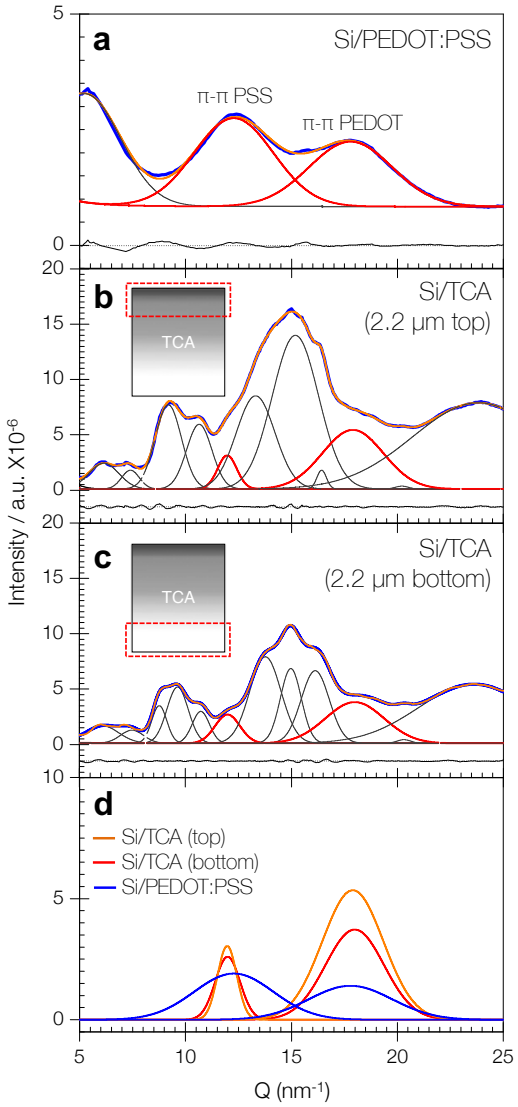


**Figure 6.** Radial integrated GIWAXS diffractograms of bare TCA-top (2.2 μm scattering-depth), TCA-bottom (2.2 μm scattering-depth) and pristine PEDOT:PSS (2.4 μm scattering-depth); **a**, **b** and **c**, respectively. The blue solid line corresponds to the experimental value and the orange solid lines correspond to the addition of all the fit peaks. Fitted corresponding peaks for π-π PSS (left peak) and π-π PEDOT (right peak) for each sample are shown in **d**. All data are corrected for measurement time and intensity fluctuations of the primary X-ray beam.

## Conclusions

We developed an innovative manufacturing alternative for the fabrication of perovskite/silicon monolithic tandem solar cells based on the lamination of individual sub-cells. A PEDOT:PSS-assisted transparent-conductive adhesive composite was utilized, for the first time, as interconnection layer system yielding devices with fill factors of up to 80.4% and steady-state efficiencies of up to 21.0%. The fill factor of our monolithic tandem exceeds state-of-the-art technologies based on much more elaborate fabrication protocols. Given the simplicity of our fabrication protocol, particularly, the possibility of designing sub-cells independently, we anticipate that a similar approach could be used to realize other heterojunction tandem structures, for instance, by exploring organic semiconducting blends from solution to further tune the absorption complementarity with perovskite, silicon and other semiconductors.

An important aspect of this work relies in the molecular understanding of the functionality of D-sorbitol doped PEDOT-PSS. D-sorbitol interacts mainly with PSS via hydrogen bonds to indirectly enhance the orientation of PEDOT chains (conformational doping). This happens predominantly at the top of the D-PEDOT-PSS layer – the junction between both sub-cells – because D-sorbitol tends to diffuse towards the surface to induce π-π stacking of PEDOT. This phenomenon is likely to dominate the necessary mechanical adhesion for good electrical contact.

While these results underscore the importance of transparent conductive adhesives for the fabrication of photovoltaic tandem structures, it also paves the way for new science to be explored in connection with the nature of the electrical contact at the interface of the interconnection layer. Specifically, future work will have to provide a fundamental understanding of how molecular interactions at the interface relate to the electronic performance of the interconnection layer and the full device. We believe that such understanding will further advance the performance of transparent conductive adhesives based on PEDOT:PSS, not only for the field of photovoltaics but across many other applications where benign, water processable materials with advanced functionality play a critical role.

## Materials and methods

***Materials and solutions:*** Unless stated otherwise, all materials were used as received and were purchased by Merck or Aldrich. $CH_3NH_3I$ was purchased from Dyenamo. PEDOT:PSS PH1000 and sorbitol were acquired from Heraeus and Sigma-Aldrich, respectively. A 40wt% blend of PEDOT:PSS and sorbitol was stirred overnight at 60ºC. PTAA polymeric material was purchased from Lumtec. A 3mg/mL solution in Chlorobenzene was stirred at 60ºC overnight. A 12 wt.% of CuSCN in diethyl sulphide was stirred at room temperature over-night. ZnO:Al nanoparticles dispersion was provided by Avantama; anhydrous solvents and short exposures to air were used during its preparation. Branched PEI solution (50% in $H_2O$) was purchased from Sigma-Aldrich. $PbI_2$ and $CH_3NH_3I$ mixed with mole ratio of 1:1 with concentration of ~40wt.% a mixture of DMF and DMSO (2:1 v/v). The precursor was stirred at 60ºC for 20 minutes and subsequently filtered while still warm. Prior to utilization, the precursor solution was stored in the dark for at least 24 hours.

***Perovskite device fabrication:*** For the perovskite, sub-cell fabrication, laser patterned ITO (with a roughness of 5-7 nm RMS) substrates were ultra-sonic bath cleaned using acetone and isopropanol for 10 minutes each followed by an oxygen plasma cleaning process. The cleaned substrate was then coated with a PTAA layer by means of spin coating at a speed of 3000 rpm and annealed at 120ºC for 15 minutes. The CuSCN solution was spin coated at 3000 rpm and annealed at 110ºC for 10 minutes. The perovskite deposition was performed by spin casting ~90 μL of the precursor on the selective contact layer at various speeds. Right after deposition, the wet film was partially dried with a moderately strong nitrogen stream within 10 seconds. The partially dry perovskite film was annealed at 110ºC for 10 minutes. After perovskite deposition, a compact ~60 nm thick layer of $PC_{60}BM$ is spin coated. A 2 wt.% solution of $PC_{60}BM$ in Chlorobenzene is then deposited using a three-step speed profile with no subsequent annealing. The ZnO:Al film was spin coated at 2000 rpm and annealed during 5 minutes at 80 ºC. PEI was spin coated at 1000 rpm and annealed at 80 ºC. For the opaque devices, the counter electrode was deposited through a shadow mask by thermal evaporation under a vacuum of $10^{-6}$ Torr. The device area for the opaque perovskite-based devices is 10.4 $mm^2$.

***Silicon device fabrication:*** The silicon heterojunction solar cells were processed using 3 Ωcm n-type (100) silicon wafers, which were RCA cleaned. An HF dip (2min, 1%) was performed be-

fore each amorphous silicon deposition. Intrinsic and doped amorphous silicon layers were deposited using RF (13.56 MHz) plasma enhanced chemical vapour deposition with silane and hydrogen. Additionally, diborane and phosphine were used for p- and n-type doping respectively. 5 nm thick intrinsic amorphous silicon layers were deposited at a temperature of 170°C, a pressure of 1.5 mbar, with gas flows of 60 sccm silane and 135 sccm hydrogen, with an electrode distance of 12.7 mm and a plasma power density of 14 $mW/cm^2$. Additionally, the intrinsic layer was treated with a hydrogen plasma at 170°C, 1 mbar, for 90 s, with a hydrogen flow of 150 sccm at an electrode distance of 25 mm directly after deposition. 10 nm thick p-type doped amorphous silicon layers were deposited at a temperature of 170°C, a pressure of 3 mbar, with gas flows of 60 sccm silane, 144 sccm hydrogen and 48 sccm of diborane (1% in hydrogen), with an electrode distance of 19 mm and a plasma power density of 10.5 $mW/cm^2$. 12 nm thick n-type doped amorphous silicon layers were deposited at a temperature of 210°C, a pressure of 2 mbar, with gas flows of 40 sccm silane, 170 sccm hydrogen and 8 sccm of phosphine (1% in hydrogen), with an electrode distance of 12.7 mm and a plasma power density of 14 $mW/cm^2$. ITO layers were deposited using RF-sputtering from a ceramic target at a substrate temperature of 50°C, a pressure of $3x10^{-3}$ mbar, 0.2% oxygen in argon as sputter gas and a RF power of 200 W. ITO layer thicknesses were about 43 nm for the front side layers and about 90 nm for the back-side layers. The back-side metal contact was formed by thermal evaporation of 10 nm titanium followed by 500 nm of silver.

***ICL deposition and lamination:*** PEDOT:PSS-sorbitol blend along with AgNW ink were deposited through doctor blade. A ~100 nm layer of AgNW is coated on top of the ITO electrode from the silicon cell. After drying the films for 3 minutes at 80ºC we proceed with the deposition of our PEDOT:PSS-sorbitol blend (40wt%). Approximately 3 µm of the PEDOT:PSS-sorbitol blend was deposited on top of the AgNW. The resulting ICL-silicon sub-cell was then dried for 3 minutes at 120ºC. During the last 30 seconds, we preheated our perovskite sub-cells at 120ºC and immediately pressed the sub-cells against each other for a short time.

***Device Characterization:*** Current density-voltage (*J-V*) characterization under light was carried out by means of a Keithley 2400 source measure unit (SMU) and Newport Sol1A solar simulator with an AM1.5 G spectrum at 0.1 $W/cm^2$, which was determined by a calibrated single-crystal standard Si-cell. To avoid current contribution from adjacent pixels during the measurement we

utilized a shadowing mask for all *J-V* characterizations. *J-V* characterization was carried out as follows: forward direction, speed: 1 mV $ms^{-1}$ and a dwell time of 8 ms. Opaque single-junction and tandem devices were initially tested with the aid of a maximum power point tracker based on a perturb-and-measure routine and/or uninterrupted current density sampling under initial $V_{mpp}$ conditions. All reported *J-V* characterizations were obtained after efficiency stabilization for at least 1 minute. To neglect any spectral mismatch, the lamp was calibrated according to the integrated photocurrent from the EQE measurements. External quantum efficiency spectra were recorded with an Enli Technology QE-R measurement system, also calibrated with a Si PV cell, data was averaged over 25 measurements for each point. In the case of the tandem devices, we isolated each sub-cell optoelectrically in order to obtain an EQE spectrum. To light bias the silicon sub-cell we utilized an 850-nm laser diode. To light bias the perovskite sub-cell we utilized a 450-nm laser line. ThorLabs provided both laser diodes. Optical absorption measurements were performed with a UV-Vis spectrometer Lambda 950 from Perkin equipped with an integrating sphere.

***Optical Simulation:*** Except for PTAA and CuSCN, all the optical constants where estimated as follows: Reflection (incidence angle of 8°) and transmission (normal to the sample) of the deposited layers are measured and implemented to the software NIKA[47] in order to obtain the wavelength-dependent complex refractive index. Furthermore, the ICL layer is treated as an effective medium in the framework of the TMF method. As such, optical constants were extracted from the software NIKA and the nominal thickness was verified by experimental measurements.

***Hyperspectral global imaging****:* Hyperspectral imaging provides spectrally resolved images and can help identify and quantify inhomogeneities in a given sample. Photoluminescence hyperspectral data was acquired using Photon etc's IMA™ system. This system is based on Bragg tunable filters. This technology acquires monochromatic images of the entire field view. IMA™ consists of a hyperspectral filter coupled with a microscope. A beam shaping module is required to provide uniform global illumination over the entire field of view. A 532 nm laser is used to excite the sample and the signal is detected with a Si CCD camera. Photoluminescence images were acquired with a spectral resolution ~ 2 nm and a spatial resolution ~ 2 µm. A 50X objective was used to image an area of 135 µm x 180 µm with a fluence of 0.066 $\mu W/\mu m^2$. PL images were acquired from 620 nm to 850 nm and the the total acquisition time was less than 2 minutes. The isopotential created when using global illumination prevents charge diffusion towards the

darker regions of the sample. Hence, global imaging allows carrying PL within the range of realistic operating mode of solar cells.

***GIWAXS:*** Grazing Incidence X-Ray Diffraction (GIXD) gives access to the in-plane and out-of-plane structure of crystalline thin films. The GIXD diffractograms were collected with the highly customized Versatile Advanced X-ray Scattering instrumenT ERlangen (VAXSTER) at the Institute for Crystallography and Structural Physics (FAU, Germany). The instrument is equipped with a 9.24 keV MetalJet D2 70 kV X-ray source (EXCILLUM, Sweden), a focusing 150 mm Montel optics (INCOATEC, Germany) and a fully evacuated beam path. Three of the available four double-slits were used, with the last two double-slit systems being equipped with low scattering silicon slits (JJXray/SAXSLAB, Denmark). Aperture sizes of the first two beam-shaping double-slit systems were 0.7×0.7 $mm^2$ and 0.462×0.462 $mm^2$, respectively. The last double-slit system was used for absorbing slit scattering and was set to 1.0×1.0 $mm^2$. A 2D hybrid-pixel Pilatus 300K detector (Dectris, Switzerland) was used to collect the scattered radiation. The samples were mounted in vacuum on a yz-theta goniometer allowing to adjust grazing incidence angles, which maximizes the scattering volume and thus enhances the scattered intensity. The incidence angle was set to 0.17°, which is in between the critical angles of the PEDOT:PSS layer and the silicon substrates. This angle is used here to enhance the scattered intensity by maximization of the scattering sample volume and minimizing the background scattering from the substrate. The detector-to-sample distance (SDD) was calibrated with a silver behenate standard and was set to 173 mm for the measurements of non-flipped PEDOT:PSS + Sorbitol, 175 mm for the measurements of pure Sorbitol and 178 mm for all other GIXD measurements. Data were reduced by radial integration using the software dpdak[52].

## References


1. National Center for Photovoltaics (NCPV) at the National Renewable Energy Laboratory (NREL). (2017). Available at: www.nrel.gov/pv/assets/images/efficiency-chart.png. (Accessed: 23rd November 2017)

2. Hou, Y. *et al.* A generic interface to reduce the efficiency-stability-cost gap of perovskite solar cells. *Science* **5561,** 1–10 (2017).

3. Arora, N. *et al.* Perovskite solar cells with CuSCN hole extraction layers yield stabilized efficiencies greater than 20 %. *Science* **5655,** 1–9 (2017).

4. Goodrich, A. C., Powell, D. M., James, T. L., Woodhouse, M. & Buonassisi, T. Assessing the drivers of regional trends in solar photovoltaic manufacturing. *Energy Environ. Sci.* **6,** 2811 (2013).

5. Bush, K. A. *et al.* 23.6%-Efficient Monolithic Perovskite/Silicon Tandem Solar Cells With Improved Stability. *Nat. Energy* **2,** 17009 (2017).

6. Werner, J. *et al.* Efficient Monolithic Perovskite/Silicon Tandem Solar Cell with Cell Area >1 cm2. *J. Phys. Chem. Lett.* **7,** 161–166 (2016).

7. Spyropoulos, G. D. *et al.* Flexible organic tandem solar modules with 6% efficiency: combining roll-to-roll compatible processing with high geometric fill factors. *Energy Environ. Sci.* **7,** 3284–3290 (2014).

8. Ouyang, J. & Yang, Y. Conducting polymer as transparent electric glue. *Adv. Mater.* **18,** 2141–2144 (2006).

9. Nevrela, J. *et al.* Secondary Doping in Poly (3, 4-ethylenedioxythiophene):Poly ( 4-styrenesulfonate) Thin Films. *J. Polym. Sci. part B Polym. Phys.* 1139–1146 (2015).

10. Nardes, A. M. *et al.* Conductivity , work function , and environmental stability of PEDOT : PSS thin films treated with sorbitol. *Org. Electron.* **9,** 727–734 (2008).

11. Janssen, A. J., Kemerink, M., Alexandre, B. & Nardes, M. A Morphological Model for the Solvent-Enhanced Conductivity of PEDOT : PSS Thin Films. *Adv. Funct. Mater.* 865–871 (2008).

12. Ouyang, L., Musumeci, C., Jafari, M. J. & Ederth, T. Imaging the Phase Separation Between PEDOT and Polyelectrolytes During Processing of Highly Conductive PEDOT:PSS Films. *ACS Appl Mater Interfaces* 19764−19773 (2015).

13. Rivnay, J. *et al.* Structural control of mixed ionic and electronic transport in conducting polymers. *Nat. Commun.* **7,** 11287 (2016).

14. Palumbiny, C. M. *et al.* The crystallization of PEDOT:PSS polymeric electrodes probed in situ during printing. *Adv. Mater.* **27,** 3391–3397 (2015).

15. Shi, H., Liu, C., Jiang, Q. & Xu, J. Effective Approaches to Improve the Electrical

Conductivity of PEDOT:PSS: A Review. *Adv. Electron. Mater.* **1,** 1–16 (2015).

16. Huang, J., Li, G. & Yang, Y. A semi-transparent plastic solar cell fabricated by a lamination process. *Adv. Mater.* **20,** 415–419 (2008).

17. Shimada, C. & Shiratori, S. Viscous conductive glue layer in semitransparent polymer-based solar cells fabricated by a lamination process. *ACS Appl. Mater. Interfaces* **5,** 11087–11092 (2013).

18. Bryant, D. *et al.* A transparent conductive adhesive laminate electrode for high-efficiency organic-inorganic lead halide perovskite solar cells. *Adv. Mater.* **26,** 7499–7504 (2014).

19. Makha, M. *et al.* Ternary semitransparent organic solar cells with a laminated top electrode. *Sci. Technol. Adv. Mater.* **18,** 68–75 (2017).

20. Spyropoulos, G. D. *et al.* Organic and perovskite solar modules innovated by adhesive top electrode and depth-resolved laser patterning. *Energy Environ. Sci.* **9,** 2302–2313 (2016).

21. Stolterfoht, M. *et al.* Approaching the fill factor Shockley-Queisser limit in stable, dopant-free triple cation perovskite solar cells. *Energy Environ. Sci.* **10,** 1530–1539 (2017).

22. Chen, B. *et al.* Efficient Semitransparent Perovskite Solar Cells for 23.0%-Efficiency Perovskite/Silicon Four-Terminal Tandem Cells. *Adv. Energy Mater.* **6,** 1601128 (2016).

23. Duong, T. *et al.* Rubidium Multication Perovskite with Optimized Bandgap for Perovskite-Silicon Tandem with over 26% Efficiency. *Adv. Energy Mater.* **7,** 1–11 (2017).

24. Yang, W. S. *et al.* High-performance photovoltaic perovskite layers fabricated through intramolecular exchange. *Science* **348,** 1234–1237 (2015).

25. Fu, F. *et al.* High-efficiency inverted semi-transparent planar perovskite solar cells in substrate configuration. *Nat. Energy* **2,** 16190 (2016).

26. Ingram, I. D. V., Tate, D. J., Parry, A. V. S., Sprick, R. S. & Turner, M. L. A simple method for controllable solution dcoping of complete polymer field-effet transistors. *Appl. Phys. Lett.* **104,** 153304 (2014).

27. Jaffe, J. E. *et al.* Electronic and defect structures of CuSCN. *J. Phys. Chem. C* **114,** 9111–9117 (2010).

28. Albrecht, S. *et al.* Towards optical optimization of planar monolithic perovskite / silicon-heterojunction tandem solar cells. *J. Opt.* **18,** 1–10 (2016).

29. Grant, D. T., Catchpole, K. R., Weber, K. J. & White, T. P. Design guidelines for perovskite / silicon 2- terminal tandem solar cells : an optical study. *Opt. Express* **24,** 1454–1470 (2016).

30. Wijeyasinghe, N. *et al.* Copper(I) Thiocyanate (CuSCN) Hole-Transport Layers Processed from Aqueous Precursor Solutions and Their Application in Thin-Film Transistors and Highly Efficient Organic and Organometal Halide Perovskite Solar Cells. *Adv. Funct. Mater.* **27,** 1–13 (2017).

31. Marchioro, A. *et al.* Unravelling the mechanism of photoinduced charge transfer processes in lead iodide perovskite solar cells. *Nat. Photonics* 1–6 (2014). doi:10.1038/nphoton.2013.374

32. Stranks, S. D. *et al.* Electron-Hole Diffusion Lengths Exceeding 1 micrometer in an irganometal trihalide perovskite absorber. *Science* **342,** 341–344 (2014).

33. Franz, U. The long-wavelength edge of photographic sensitivity and of the electronic absorption of solids. *Phys. Rev.* 1324 (1953).

34. De Wolf, S. *et al.* Organometallic halide perovskites: Sharp optical absorption edge and its relation to photovoltaic performance. *J. Phys. Chem. Lett.* **5,** 1035–1039 (2014).

35. McMeekin, D. P. *et al.* A mixed-cation lead mixed-halide perovskite absorber for tandem solar cells. *Science* **351,** 151–155 (2016).

36. Zhang, W. *et al.* Enhanced optoelectronic quality of perovskite thin films with hypophosphorous acid for planar heterojunction solar cells. *Nat. Commun.* **6,** 10030 (2015).

37. Elschner, A., Kirchmeyer, S., Lövenich, W., Merker, U. & Reuter, K. *PEDOT; Principles and Applications of an Intrinsically Conductive Polymer*. (CRC Press, 2011).

38. Fesser, K., Bishop, A. R. & Campbell, D. K. Optical absorption from polarons. *Phys. Rev.* **27,** (1983).

39. Bredas, J. L. & Street, G. B. Polarons, Bipolarons, and Solitons in Conducting Polymers. *Acc. Chem. Res.* **18,** 309–315 (1985).

40. Havinga, E. E., Mutsaers, C. M. J. & Jenneskens, L. W. Absorption Properties of Alkoxy-Substituted Thienylene−Vinylene Oligomers as a Function of the Doping Level. *Chem. Mater.* **8,** 769–776 (1996).

41. Hwang, J., Tanner, D., Schwendeman, I. & Reynolds, J. Optical properties of nondegenerate ground-state polymers: Three dioxythiophene-based conjugated polymers. *Phys. Rev. B* **67,** 1–10 (2003).

42. Heuer, H. W., Wehrmann, R. & Kirchmeyer, S. Electrochromic window based on conducting poly (3,4-ethylenedioxythiophene)poly(styrene sulfonate). *Adv. Funct. Mater.* **12,** 89–94 (2002).

43. Khasim, S., Pasha, A., Roy, A. S., Parveen, A. & Badi, N. Effect of Secondary Doping Using Sorbitol on Structure and Transport Properties of PEDOT – PSS Thin Films. *J. Electron. Mater.* (2017). doi:10.1007/s11664-017-5437-5

44. Chiu, W. W., Travaš-Sejdić, J., Cooney, R. P. & Bowmaker, G. A. Spectroscopic and conductivity studies of doping in chemically synthesized poly(3,4-ethylenedioxythiophene). *Synth. Met.* **155,** 80–88 (2005).

45. Reyes-Reyes, M., Cruz-Cruz, I. & López-Sandoval, R. Enhancement of the electrical

conductivity in PEDOT: PSS films by the addition of dimethyl sulfate. *J. Phys. Chem. C* **114,** 20220–20224 (2010).

46. Chiu, W. W., Travaš-Sejdić, J., Cooney, R. P. & Bowmaker, G. A. Studies of dopant effects in poly(3,4-ethylenedioxythiophene) using Raman spectroscopy. *J. Raman Spectrosc.* **37,** 1354–1361 (2006).

47. De Kok, M. M. *et al.* Modification of PEDOT:PSS as hole injection layer in polymer LEDs. *Phys. Status Solidi Appl. Res.* **201,** 1342–1359 (2004).

48. Xia, Y., Zhang, H. & Ouyang, J. Highly conductive PEDOT:PSS films prepared through a treatment with zwitterions and their application in polymer photovoltaic cells. *J. Mater. Chem.* **20,** 9740 (2010).

49. Barnett, R. M., Georgi, H. & Politzerj, H. D. Depth-Controlled Grazing-Incidence Diffraction of Synchrotron X Radiation. *Phys. Rev.* **37,** 1313–1316 (1976).

50. Takano, T., Masunaga, H., Fujiwara, A., Okuzaki, H. & Sasaki, T. PEDOT Nanocrystal in Highly Conductive PEDOT_PSS Polymer Films. *Macromolecules* 3859−3865 (2012).

51. Palumbiny, C. M. *et al.* Molecular reorientation and structural changes in cosolvent-treated highly conductive PEDOT:PSS electrodes for flexible indium tin oxide-free organic electronics. *J. Phys. Chem. C* **118,** 13598–13606 (2014).

52. Benecke, G. *et al.* A customizable software for fast reduction and analysis of large X-ray scattering data sets: Applications of the new DPDAK package to small-angle X-ray scattering and grazing-incidence small-angle X-ray scattering. *J. Appl. Crystallogr.* **47,** 1797–1803 (2014).

## Acknowledgements

The Cluster of Excellence funded this work through "Engineering of Advanced Materials" (EAM). The authors acknowledge financial support from the DFG research-training group GRK 1896 at Erlangen University and from the Joint Project Helmholtz-Institute Erlangen Nürnberg (HI-ERN) under project number DBF01253, respectively. C.J.B. acknowledges the financial support through the "*Aufbruch Bayern*" initiative of the state of Bavaria (EnCN and Solar Factory of the Future) and the "Solar Factory of the Future" with the Energy Campus Nürnberg (EnCN). S.L. Acknowledges the *Real Colegio Complutense* in Harvard for a Research Grant, and to the *Spanish Ministerio de Ciencia e Innovación* for a Fellowship through the *Salvador de Madariaga* Program. L.M.R and A.A.-G. acknowledge support from Tata Sons Limited - Alliance Agreement (A32391). The computations in this paper were done on the Odyssey cluster supported by the FAS Division of Science, Research Computing Group at Harvard University, and on the Arran cluster supported by the Health Sciences Platform (HSP) at Tianjin University. C.O.R.Q. would like to acknowledge M. Möhrensen for his assistance in graphic design. Similarly, C.O.R.Q would like to acknowledge Gebhard Matt and Ievgen Levchuk for helpful discussion. G.A. acknowledges the FAU for the Emerging Talents Initiative (ETI) grant #WS16-17_Nat_04. G.A. would like to acknowledge Vicent Lloret for his assistance with the experimental work. B. R., L.K., S.A. and G.C. acknowledge support from BMWi through the "PersiST" project (grant no. 0324037C). S.A. acknowledges funding by the BMBF within the project "Materialforschung für die Energiewende" for his Young Investigator Group (grant no. 03SF0540). T. A. gratefully acknowledges the financial support of the Solar Technologies go Hybrid (SolTech) and Bavarian Equal Opportunities Sponsorship – Förderung von Frauen in Forschung und Lehre (FFL). C.O.R.Q would like to gratefully acknowledge the financial support from The Mexican National Council for Science and Technology (CONACYT).

## Author Contributions

C.O.R.Q. wrote the manuscript with comments from all co-authors and highlighted contributions from M.S. C.O.R.Q. coordinated and performed photovoltaic device fabrication. C.O.R.Q. coordinated all experiments, measurements and simulations. G.D.S. assisted with the tandem lamination process. C.O.R.Q. and K.F. performed optical simulations. M.S., G.D.S., N.L., T.A. and A-A.G. assisted with data interpretation, story layout design and contributed ideas. C.O.R.Q., N.S. and E.S. contributed with the electron microscopy analysis. C.O.R.Q., M.B. and T.B. contributed with X-ray studies. C.O.R.Q., G.A., F.H. and A.H. contributed with Raman studies. L.-I. D.-B. and N.G. assisted with PL measurements. N.G. and A.C. assisted with FTPS and PL data analysis and interpretation. M.M, G.C., L.K., B.R., and S.A. Provided silicon cells. QM/DFT calculations and analysis were performed by L.M.R. MD parametrization was done by S.L., and MD simulations were performed and analysed by S.L. and J.D.P. C.J.B. supervised the project.